^{17}O hyperfine spectroscopy in surface chemistry and catalysis

Yu-Kai Liao [a,b,1], Paolo Cleto Bruzzese [b,a,1], Enrico Salvadori [a], Mario Chiesa [a,*]

[a] Department of Chemistry and NIS Centre of Excellence, University of Turin, via Giuria 9, 10125 Torino, Italy
[b] Felix Bloch Institute for Solid State Physics, Leipzig University, Linnéstr. 5, 04103 Leipzig, Germany

ARTICLE INFO

ABSTRACT

Oxide-based materials are of key technological importance in different areas including advanced functional materials, solid state chemistry and catalysis. Many of the key questions concerning these areas involve understanding the chemical bond between the metal and the oxygen ions in the first or subsequent coordinating shells. The spectroscopic study of oxygen is therefore of fundamental importance to elucidate the complex interfacial coordination chemistry that underlies the development of metal-oxide supported catalysts and other advanced materials. Oxygen atoms at solid surfaces or lining the pores of zeolite frameworks play a vital role in stabilizing and defining the electronic and geometric structure of single metal atoms or clusters that act as catalytically active sites. In the case of paramagnetic species, EPR and its related hyperfine techniques offer a unique opportunity to explore and understand the nature of the chemical bonding in metal-oxide systems through the detection of the ^{17}O hyperfine interaction. In this perspective we offer an overview of experimental considerations and relevant examples specific to ^{17}O hyperfine spectroscopy of transition metal ions in zeolites relevant to catalysis. ^{17}O hyperfine coupling values are obtained, which allow discriminating σ- and π-bonding channels in metal-oxygen bonds involving first-row transition metal ions. An exhaustive collection of ^{17}O hyperfine and nuclear quadrupole couplings in different systems including molecular and biomolecular chemistry is provided, emphasizing the connection between interfacial and molecular inorganic coordination chemistry.

1. Introduction

Heterogeneous catalysts based on metal particles dispersed on a support are central in a high number of important industrial reactions. The dispersion of the metal particles on a solid such as an oxide, a zeolite or a carbonaceous material allows to increase the number of atoms of the catalytically active phase which is accessible to reactant molecules. However, the function of the solid support is much more than this. Although for quite a long time the role of the solid has been merely interpreted as that of a dispersing medium inert from a chemical point of view, it has now become clear that a given support is potentially capable of influencing the size and the electronic structure of the supported metals [1]. The most dramatic effects are observed when isolated atoms are well-dispersed on the solid substrate, leading to nanostructured solids that integrate single atomic species, frequently referred to as "single metal atom catalysts" [2]. Understanding how the electronic properties of a metal are affected by the interaction of the ligands is the essence of the inorganic chemistry enterprise. What happens when the

ligand is an extended surface? This question is central to the design and implementation of state-of-the-art functional materials containing transition metals. The rearrangement of the atomic levels of the surface-bound isolated atom is in fact related to ligand effects, which ultimately modulate the nature of the chemical interaction between the atom and the support. Depending on the nature of the ligand-support bonding and local coordination environment, single metal species interact with surface atoms forming new bonds at the interface, which can range from weak interactions, dominated by dispersive forces and polarization effects, to covalent bonds, involving the mixing of metal and oxide orbitals, up to net electron transfer interactions resulting in ionic bonds (see Fig. 1).

The number of methods intrinsically capable to monitor the formation of chemical bonds between metal atoms and surfaces in terms of charge delocalization is, however, limited. Even exquisitely surface-sensitive techniques such as XPS and, less frequently, scanning tunneling spectroscopy (STS) yield results that are not always unambiguous [3]. Nuclear spins constitute an excellent source of information

---

about the atomic scale. Due to their selectivity and sensitivity, Electron Paramagnetic Resonance (EPR) and the associated hyperfine techniques of Electron Nuclear Double Resonance, Electron Spin Echo Modulation and Electron-Electron Double Resonance (ELDOR)-detected NMR (hereafter ENDOR, ESEEM and EDNMR, respectively) can be the key to find the "needle in the haystack" when the single atoms of interest are paramagnetic. This is often the case in at least one oxidation state encountered during a catalytic cycle. Recently, the combination of electron spin resonance and scanning tunneling microscopy (ESR-STM) has opened a novel platform to access individual nuclear spins of atoms on well-defined surfaces [4–7]. However, EPR can be used, and indeed has been abundantly exploited, in bulk experiments on polycrystalline materials to investigate isolated atoms or ions [8–12]. Initiated by the seminal three-pulse ESEEM work of Kevan [13], it was soon realized that hyperfine spectroscopy can reveal crucial structural information about the metal catalyst environment. Moreover, the combination with quantum chemical computations allows the conversion of hyperfine data into accurate atomistic structures [14,15]. In the case of the interaction between metals and oxide surfaces such as zeolites, ^{17}O is the most interesting target nucleus and ^{17}O hyperfine spectroscopy a unique source of information about the local binding environment around the metal to rationalize structure−property relationships [12]. This, however, requires specific ^{17}O enrichment protocols and a judicious choice of the experimental conditions.

In this Perspective, the potential of different hyperfine techniques in the study of ^{17}O enriched oxides will be discussed. We focus on zeolites since they represent an extremely important class of heterogeneous catalysts and over the years we have considered their interaction with a large variety of paramagnetic metals to understand how EPR parameters relate to electronic configuration and interfacial coordination. Therefore, rather than presenting an exhaustive overview of all existing literature on ^{17}O EPR, we highlight the possibilities and challenges of the different approaches and illustrate them with a selected number of examples taken from our recent research together with some original data.

2. Materials and methods

The H-ZSM-5 zeolite (commercial sample CBV8014, supplied by Zeolyst, Si/Al = 40) was dehydrated by thermal treatment at 673 K under dynamic vacuum (residual pressure <10–4 mbar) for two hours and subsequently calcined at 773 K in O_2 atmosphere to remove spurious organic residues.

Framework substitution of ^{16}O by ^{17}O was obtained by heating the dehydrated H-ZSM5 at 120 °C for 2 h, in presence of $H_2^{17}O$ (86% isotopic enrichment) vapors.

Zn- and Cd-loaded ZSM-5 were prepared by in situ sublimation of the metals on the ^{17}O enriched H-ZSM-5 zeolite. The activated zeolite was exposed for 2 min to the metal vapours and subsequently photo-irradiated with UV/Vis light with a 1500 W xenon lamp (New Port Instruments). The metal content was estimated to be of the order of 2% wt by energy dispersive X-ray spectroscopy (EDS), with a scanning electron microscopy FEI Quanta 200 FEG-ESEM equipped with an EDAX EDS detector.

V doping was achieved by an anhydrous vapour exchange process at room temperature. The ^{17}O-enriched zeolite was exposed to the VCl_4 vapours in a quartz cell equipped with an EPR tube. The cell was evacuated after the reaction to remove excess VCl_4 and the reaction products (HCl).

X-band (microwave frequency 9.46 GHz) CW EPR spectra were performed on a Bruker EMX spectrometer equipped with a cylindrical cavity. A modulation frequency of 100 kHz, a modulation amplitude of 0.2 mT, and a microwave power of 0.02 mW were used. Q-band (microwave frequency 33.7 GHz) CW-EPR experiments were performed on a Bruker ELEXYS 580 EPR spectrometer, equipped with helium gas-flow cryostat from Oxford Inc. All samples were introduced in the EPR tubes in a glove box (O_2 < 0.5 ppm, H_2O < 0.5 ppm) and sealed in order to avoid contact with the atmosphere.

Electron-spin-echo (ESE) detected EPR spectra were recorded with the pulse sequence π/2−τ−π−τ−echo. Pulse lengths $t_{\pi/2}$ = 16 ns and t_π = 32 ns, a τ value of 200 ns. Hyperfine Sublevel Correlation (HYSCORE) experiments were carried out with the pulse sequence π/2-τ-π/2-t_1-π-t_2-π/2-τ-echo, applying a eight-step phase cycle for eliminating unwanted echoes. Microwave pulse lengths $t_{\pi/2}$ = 16 ns, t_π = 32 ns were used the interpulse delay τ value for each spectrum is reported in the figure captions. The time traces of the HYSCORE spectra were baseline corrected with a third-order polynomial, apodized with a Hamming window and zero filled. After two-dimensional Fourier transformation, the absolute value spectra were calculated.

Q-band Davies ENDOR spectra were recorded using the pulse sequence π-T- π/2- τ- π-τ-echo with t_π = 32 ns and $t_{\pi/2}$ = 16 ns, $t_{\pi RF}$ = 14 μs, T = 16 μs and τ = 200 ns. The use of unselective microwave pulses suppresses the small hyperfine couplings in favour of large ones. All EPR spectra were simulated employing the Easyspin package [16].
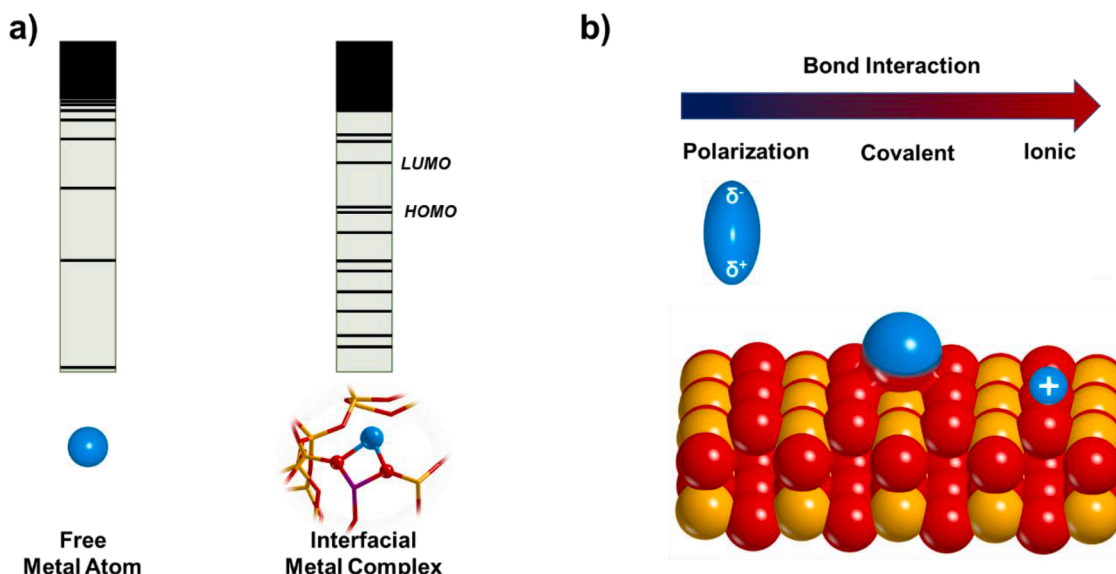

Fig. 1. Schematic illustration of a) electronic structure of isolated and supported single metal atoms; b) most relevant type of metal-support interactions.

Periodic model of $V^{IV}O$/ZSM-5 and Cu^{II}/ZSM-5 were built starting from purely siliceous Silicalite-1 MFI structure (as refined by Artioli and co-workers [17]) by replacing two T8 sites of the same six-membered ring (γ-ring) by two Al atoms. The excess of negative charge was exactly compensated by introducing one $V^{IV}O^{2+}$ group or Cu^{II} cation inside such ring, close to the Al sites (space group *P1*). Geometry optimization of the periodic models were performed by using the massive parallel version of CRYSTAL17 code (MPPCRYSTAL) [18–20] in the frame of Density Functional Theory (DFT) adopting the hybrid B3LYP method, Becke's three parameters exchange functional and the correlation functional from Lee, Yang and Parr [21,22]. Dispersive interactions were taken into account empirically through the so-called DFT-D3 method in conjunction with a three-body correction [23,24]. Pob-TZVP-rev2 basis set was adopted for all the elements [25]. Further computational details concerning periodic calculations are described elsewhere [14,15].

Molecular cluster calculations were carried out with Orca code (v5.0.3) [26] to compute ^{17}O hyperfine couplings. $V^{IV}O$/ZSM-5 and Cu^{II}/ZSM-5 cluster models were cut out from the related optimized periodic structure and the dangling bonds were saturated with hydrogen atoms orientated along the broken bonds. No further geometry optimization was performed in order to maintain the same relaxed atomic coordinates as in the optimized periodic structure. The net charge on the molecular models was set to 0 in a doublet spin state. The B3LYP functional in conjunction with CP(PPP) [27] for V atom and EPR-III [28] basis sets for the O atoms directly bound to the V were employed. All the other elements were treated with the def2-TZVP basis set [29]. The spin-orbit coupling (SOC) contribution was explicitly treated by using complete mean-field spin-orbit operator (SOMF) [30]. Increased integration grids were employed (DefGrid3) and tight energy convergence settings were applied throughout (TightSCF).

3. Results and discussion

3.1. Open-shell transition metal ions and ^{17}O enrichment of zeolite materials

Zeolites are aluminosilicates made of tetrahedral units, which are fully connected through oxygen atoms to form open, porous frameworks. Substitution of silicon by aluminium within the framework introduces a negative charge that needs to be balanced by cationic species (often called extra-framework cations) that distribute in the pores and channels of the solid. In a number of relevant cases, the extra-framework cations are transition metal ions (TMIs) featuring paramagnetic states. TMIs display a variety of coordination numbers with O^{2-} ions, which determines the stereochemistry of the interfacial complex. It is the combination of the chemistry of the framework oxide ions and extra-framework cations together with the microporous architectures that confers to metal-loaded zeolites some exceptional properties that are utilized in many different industrial applications, from heterogeneous catalysis to ion exchange.

To explore in details the interfacial coordination chemistry of TMIs in zeolites with EPR, it is therefore mandatory to recover the hyperfine interaction between the metal electron spin and oxygen nuclear spins. Due to its low natural abundance (0.038%), ^{17}O isotopic enrichment is needed. Given the high cost of ^{17}O labelling, isotopic enrichment protocols (or the adaption of existing ones), need to be developed to ensure maximum atom economy. To this end we optimized post-synthetic treatments using ^{17}O enriched water vapours. After standard zeolite activation at 673 K under dynamic high-vacuum conditions (equilibrium pressure $<10^{-4}$ mbar), the dehydrated solid (about 20 mg) is contacted at room temperature with $H_2^{17}O_{(g)}$ vapours (20 mbar) and steamed at 393 K. Under these conditions an efficient ^{17}O isotopic enrichment of the order of 70% around the metal centre is achieved, as evaluated through the intensity of ^{17}O EPR hyperfine transitions [31]. It is to note that, at variance with solid-state NMR spectroscopy where ^{17}O enrichment is

typically performed through hydrothermal exchange processes with $H_2^{17}O_{(l)}$ to achieve bulk exchange [32], the sensitivity and selectivity of EPR towards paramagnetic species require to monitor only the O atoms directly linked to the paramagnetic metal. These correspond to oxide ions surrounding Si-O-Al motives that are more easily exchanged as compared to Si-O-Si units. For this reasons, ^{17}O enrichment can be achieved with mild and atom-economic procedures.

Since this perspective is devoted to the use of EPR spectroscopy and ^{17}O labelling to derive electronic and geometrical structures of metallic ions supported on oxides, the following sections provide experimental considerations and relevant examples specific to ^{17}O hyperfine spectroscopy of TMIs in zeolites relevant to catalysis. We have chosen to make these sections free of heavy formalism but comprehensive enough to help the non-EPR reader navigating the ever-growing EPR literature.

3.2. ^{17}O hyperfine spectroscopy

^{17}O is the only stable isotope of oxygen with a nuclear quantum number of $I = 5/2$, and a negative nuclear g factor $g_O = -0.75752$. A nucleus with $I = 5/2$ with a non-zero quadrupolar interaction, coupled to one unpaired electron with $S = 1/2$ features a total of 12 energy levels at high field, six for each of the two electron spin manifolds (see Fig. 2a). Because of the associated nuclear quadrupole interaction, the energy spacing between pairs of sublevels is not even but shifted proportionally to m_I^2.

3.2.1. Continuous wave (CW-) EPR of ^{17}O enriched samples

The spin multiplicity rule, common to NMR, dictates that $2nI+1$ lines are expected for each nucleus coupled to the electron spin, where I is the nuclear spin quantum number and n is the number of magnetically equivalent nuclei. In case of a single ^{17}O nucleus, six lines with equal intensity are therefore expected, whereas two equivalent ^{17}O nuclei yield an eleven-line spectrum with relative intensities (1:2:3:4:5:6:5:4:3:2:1). Depending on the linewidth of the EPR spectrum and the magnitude of the hyperfine coupling, the isotopic enrichment either manifest as an additional broadening of the EPR line (as compared to the unlabelled sample) or as additional lines at either side of the spectrum. When the enrichment strategy does not guarantee full substitution of all ^{16}O nuclei with ^{17}O isotope, the experimental spectrum is a superposition of several sub-spectra arising from various isotopomers, namely species displaying every possible combination of the two isotopes. For instance, for an electron spin coupled to two oxygen nuclei, four isotopomers are possible: $^{16}O^{16}O$, $^{16}O^{17}O$, $^{17}O^{16}O$ and $^{17}O^{17}O$. The relative ratios, P^{nn}, follow the binomial distribution and are given by $P^{16-16} = (1 - p)^2$, $P^{16-17} = 2p(1 - p)$ and $P^{17-17} = p^2$, where p is the ^{17}O enrichment level [33], as summarized in Fig. 2b. If the ^{17}O hyperfine coupling is resolved, inclusion of all possible isotopomers in the simulation of the experimental spectra offers a way to estimate the degree of enrichment directly from EPR data, as it is shown in Fig. 3.

3.2.2. ENDOR of ^{17}O enriched samples

ENDOR monitors the actual NMR transitions induced by an incident radio frequency (RF) through the intensity change of the EPR signal. Both the RF and microwave (MW) radiations are applied during an experiment, hence the name double resonance. The most common pulsed ENDOR experiments are called Mims and Davies ENDOR, from the names of their respective inventors. Mims has greater sensitivity and it is particularly suited for small hyperfine coupling, while Davies allows the detection of arbitrary large hyperfine couplings at the cost of sensitivity [34]. In addition, Mims ENDOR suffers from so-called "blind spots" that will be addressed in the description of ESEEM and HYSCORE spectroscopies.

The ENDOR spectrum reports the relative intensity change of the EPR signal as a function of the applied RF frequency. ENDOR lines appear when the resonance condition $\nu_{ENDOR}^{\pm} = |\nu_I \pm A/2|$ is met, where ν_I is the Larmor frequency of the nucleus under investigation (given by
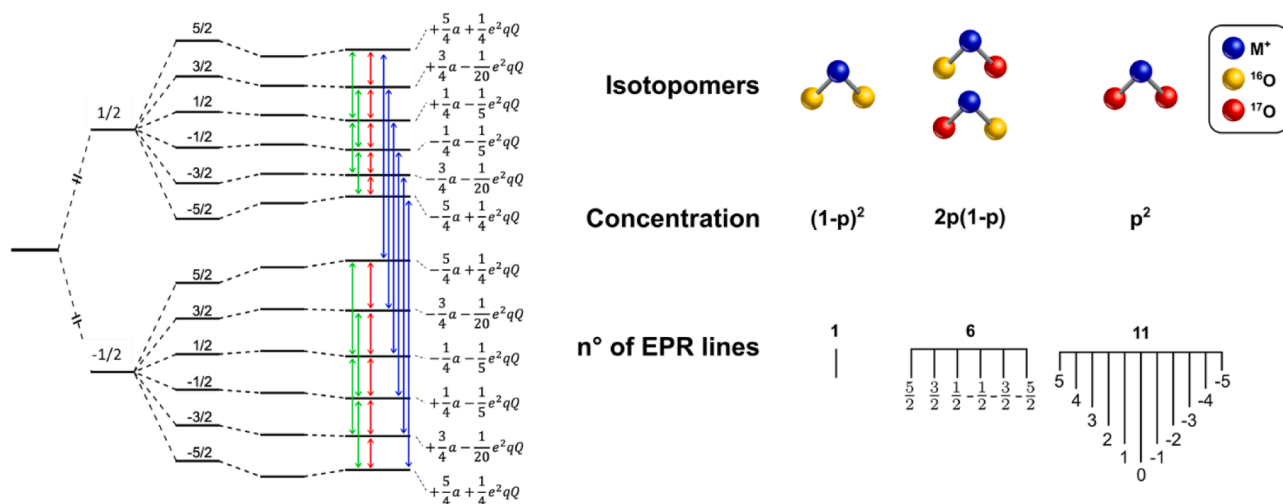
Fig. 2. a) Energy level splitting diagram for a $S = 1/2$ and $I = 5/2$ system illustrating the first-order energy level shifts due to the quadrupole interaction in the high-field regime. $e^2qQ > 0$, $\eta = 0$ and a nucleus with $g_n < 0$ are assumed. The magnetic field is assumed parallel to the z axis of the nuclear quadrupole tensor. EPR transitions are indicated in blue, NMR single-quantum transitions are in red and double-quantum NMR transitions are in green. b) Number of EPR lines and abundance of the oxygen isotopomers for a representative site involving two oxygen nuclei.
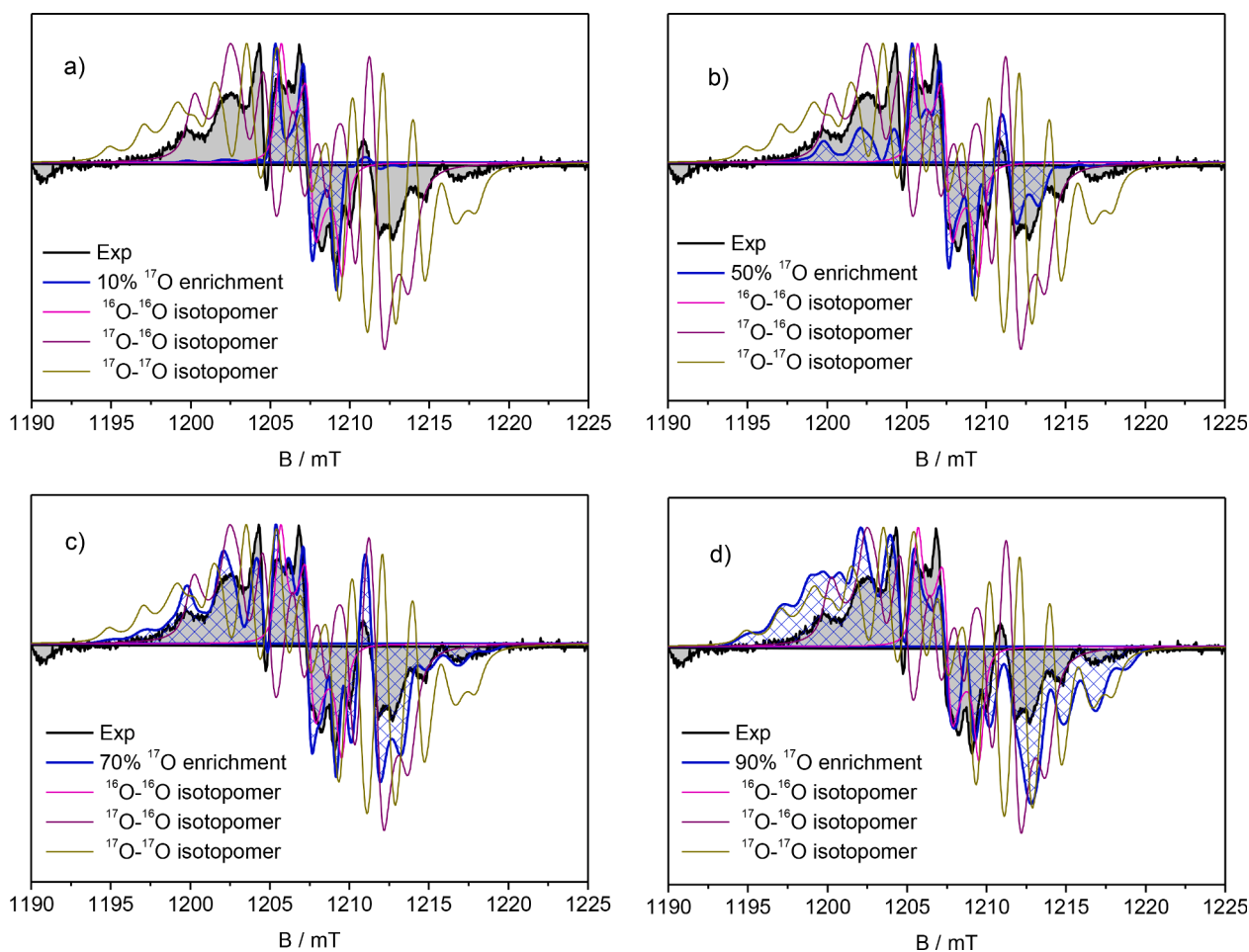

Fig. 3. Estimation of the ^{17}O enrichment around Zn^+ species in ZSM-5 through computer simulation (blue line and dashed area) of the experimental spectra (black line, grey area). The normalised individual spectral components corresponding to the three different isotopomers are also shown. The weight of each component to the sum spectrum is obtained using a binomial distribution for the % of enrichment reported on each panel. The best agreement is found assuming a local enrichment of the order of 70%. The ^{17}O hyperfine coupling tensor of ^{17}O has been derived from ^{17}O ENDOR data [14].

$\nu_I = g_n\mu_n\mathrm{B}_0/h$) and A is the orientation dependant hyperfine coupling containing both the isotropic and anisotropic contributions to the hyperfine tensor.

It is useful to distinguish between two limit scenarios called the weak-coupling and strong-coupling regimes, respectively. Considering the simple spin system $S = \frac{1}{2}$ and $I = \frac{1}{2}$, in the weak-coupling limit, the orientation dependant hyperfine coupling is less than the nuclear Larmor frequency ($\nu_I > A/2$). In this case, ENDOR lines are centred at the Larmor frequency and separated by the hyperfine coupling. On the other hand, in the strong-coupling limit, the orientation dependant hyperfine coupling is larger than the nuclear Larmor frequency ($\nu_I < A/2$), therefore ENDOR lines are centred at half the hyperfine coupling and separated by twice the Larmor frequency.

The ENDOR selection rules for a quadrupolar nucleus such as ^{17}O are modified to include the orientation dependant quadrupole coupling:

$$\nu_{ENDOR}^{\pm} \approx \left| \nu_I \pm \frac{A}{2} \pm 3P\left(m_I + \frac{1}{2}\right) \right| \tag{1}$$

where P is the effective quadrupole interaction [35]. The ENDOR spectrum for a crystal-like orientation will therefore appear as a pair of lines centred at ν_I, separated by A and additionally split into 5 lines by the quadrupole interaction [36]. These splittings are often unresolved, leading to a significant broadening of the spectra. Moreover, some of the transitions appear at too low frequencies to be detected at the conventional X-band frequencies. In addition, at this MW frequency the ^{17}O ENDOR signals often overlap with those of protons, making the interpretation of the spectra non-trivial. For these reasons higher MW frequency, when possible, offers significant advantages for the detection of ^{17}O ENDOR signals, although in favourable circumstances X- and Q-band frequencies can provide enough resolution.

3.2.3. ESEEM/HYSCORE of ^{17}O enriched samples

ESEEM indirectly monitors nuclear transitions (i.e. NMR) through EPR transitions. This is a consequence of the simultaneous excitation of forbidden and allowed EPR transitions which are coherently pumped by short and intense MW pulses and, contrary to ENDOR, it does not require the application of an additional RF field. ESEEM is intrinsically a time-domain technique and hyperfine and quadrupole interaction manifest in the primary data as modulations of the amplitude of the electron spin echo in the time domain [37]. Subsequent Fourier transformation of the experimental data gives a spectrum in the frequency domain. ESEEM is formidable at measuring hyperfine couplings that are of the order of the nuclear Larmor frequency (weak-coupling limit).

The simplest ESEEM experiment, called two-pulse (2p-) ESEEM, is based on the Hahn-echo decay pulse sequence. Hyperfine and quadrupole modulation appears superimposed to the echo decay (T_m) and are related to the nuclear transitions within an electron spin manifold. A downside of 2p-ESEEM is that combination (sum and difference) of intrinsic nuclear frequencies also appear in the frequency spectrum increasing the congestion of the experimental data.

A convenient way to eliminate combination frequencies is to resort to three-pulse (3p-) ESEEM that is based on the stimulated-echo pulse sequence. The first two $\pi/2$ pulses are kept fixed and separated by a delay τ, whereas the third $\pi/2$ pulse is applied at a variable time T and the stimulated echo appears at time τ after T. Since it depends on T_1 rather than T_m, 3p-ESEEM yields spectra with narrower lines further improving spectral resolution. However, the fixed delay τ generates a polarisation grating (with period $1/\tau$) that periodically suppresses specific nuclear frequency causing the appearance of the so-called blind-spots. Such an effect can be conveniently used to suppress certain frequency components while enhancing others.

The bi-dimensional (2D) extension of ESEEM is called HYSCORE, HYperfine Sublevel CORrElation spectroscopy. HYSCORE [38] is based on the 3p-ESEEM sequence, but a fourth unselective π pulse is added at variable time between the second and third $\pi/2$ pulses. This splits the

time T in 3p-ESEEM into two independent times which are converted into the two frequency coordinates by double Fourier transformation. It is to note that HYSCORE also suffers from the blind-spot dependence. HYSCORE improves the spectral resolution by dispersing peaks over two dimensions minimising spectral overlaps. This makes all the information buried in a mono-dimensional (1D) ESEEM experiment more accessible. A HYSCORE cross-peak represent a correlation between the frequency of a nucleus in an electron spin manifold (e.g. $m_S = +1/2$) and the frequency of the same nucleus in another spin manifold (e.g. $m_S = -1/2$). HYSCORE spectra are often reported as two back-to-back quadrants labelled (+,+) and (-,+). Nuclear spin transitions in the two different m_S manifolds are correlated to each other by non-diagonal cross-peaks, appearing at (ν_α, ν_β), (ν_β, ν_α) and (ν_α, $-\nu_\beta$), (ν_β, $-\nu_\alpha$) in the (+,+) and (+,−) quadrants, respectively. Correlation peaks appearing in the (+,+) quadrant typically arise from nuclei for which the hyperfine coupling is less than the nuclear Larmor frequency (weak-coupling). Correlation peaks in the (-,+) quadrant usually belong to nuclei for which the hyperfine interaction is greater than the Larmor frequency (strong-coupling). HYSCORE usually yields highly resolved spectra even for quadrupolar nuclei and it has become the standard experiment for the measurement of complex hyperfine and quadrupole spectra. Both ESEEM and HYSCORE obey to the same selection rules detailed in the ENDOR section. Sensitivity enhancements can be obtained by using variants of HYSCORE such as Matched HYSCORE or six-pulse (6p-) HYSCORE [20].

When the hyperfine interaction (*hfi*) and nuclear quadrupole interaction (*nqi*) are weak compared with the nuclear Zeeman interaction, approximate expressions allowing for a qualitative analysis of the frequencies of the nuclear transitions have been given by Astashkin et al. [39]. The 2D HYSCORE spectrum for a $S = 1/2$ coupled to a single ^{17}O nucleus ($I = 5/2$) theoretically consists of $2(2I)^2 = 50$ cross-peaks solely from $\Delta m_I = \pm 1$ nuclear transitions, named single-quantum transitions (shown in red in Fig. 2a). In addition, a HYSCORE spectrum should exhibit a variety of correlation peaks from $\Delta m_I = \pm 2$ or $\Delta m_I = \pm 3$ transitions, called double- and triple-quantum transitions, respectively. However, the intensity of most of the correlation peaks is very low due to the hyperfine and nuclear quadrupole anisotropies and the majority of the cross-peaks are too weak to exceed the noise level. From the large number of theoretical cross peaks, it is evident how the spread of transitions over two dimensions is a great advantage afforded by HYSCORE with respect to the 1D ESEEM. The transition frequencies of ^{17}O between the states with the nuclear spin projections $m_I = -1/2$ and $m_I = +1/2$ are those least affected by the nuclear quadrupole interaction. Therefore, these transitions are the most intense, and their frequencies are approximately (to first order in the hyperfine and nuclear quadrupole) given by $\nu = \nu_I \pm A/2$, where ν_I is the ^{17}O Zeeman frequency and A is the orientation dependant hyperfine coupling. Although the *nqi* splits each of the fundamental frequencies (ν_α and ν_β) into $2I$ different components, these splittings are usually broadened beyond detection due to the anisotropic *hfi* and/or strain effects.

The arsenal of hyperfine techniques is completed by EDNMR experiments [40]. Although not used in this work, it is worth mentioning it for the sake of completeness, as this technique has been successfully used to study metal-oxygen interactions [41]. EDNMR is a polarisation-transfer pulsed EPR technique where – at variance with ENDOR - spin forbidden transitions (involving the change of both the electron and nuclear spin projection direction) are excited using a high-turning-angle (HTA) microwave pulse [42]. Among hyperfine techniques, EDNMR is the least affected by the fast relaxation of electron spins, however suffers from poor resolution for low γ-nuclei such as ^{17}O. Successful detection of ^{17}O metal interactions has been reported at W-band [43], although recently the use of Gaussian HTA pulses proved to be very promising in the detection of ^{17}O transitions at Q band frequency [44].

Regardless of the specific experiment, an important experimental parameter is the working MW frequency and consequently the applied

magnetic field. Similar to NMR higher MW frequency improve sensitivity and increase spectral resolution allowing to better resolve each individual g-component. This is visible both in CW than in pulsed EPR. Concerning pulsed EPR, there are two additional consequences that contribute to simplify the recorded spectra. Firstly, due to the dependence of the hyperfine transitions on ν_I, a higher working frequency translates to higher spectral resolution as signals from nuclei with similar g_n are less likely to overlap. Secondly, and specifically referring to ESEEM/HYSCORE, few transitions are excited leading to a simpler spectrum. On the other hand, hyperfine modulation become shallower as the working MW frequency is increased due to difficulties associated with the simultaneous excitation of forbidden and allowed EPR transitions. From our experience, Q-band (34 GHz) represents a good compromise between spectral resolution and sensitivity for the detection of hyperfine couplings between a TMI and ^{17}O nuclei, considering the size of the Q-band EPR tubes, which allow polycrystalline powdered materials used as heterogeneous catalysts, to be studied under vacuum or controlled atmosphere.

3.3. Metal-oxygen σ-bonding. Zn^I, Cd^I and Cu^{II} in zeolites

In the course of our research, we have been focusing on the study of isolated magnetic atoms on oxide surfaces, with specific attention to their electronic properties and reactivities. An interesting example is provided by the case of monovalent metals of group 12 of the periodic table (Zn^I and Cd^I) and Cu^{II} cations stabilized in zeolites. The formation of the unusual monovalent oxidation state of Zn and Cd is promoted by electrostatic reasons. Neutral Zn or Cd atoms can reduce Brönsted acidic protons at Al-OH sites, resulting in Zn^+ [45] and Cd^+ [46] ions with a $4s^1$ and $5s^1$ electron configuration. Evaporation of Zn on a protonated zeolite leads to a narrow CW-EPR spectrum resonating at $g = 1.99$ and displaying almost unresolved anisotropy at X-band (Fig. 4a), while the three components of the **g**-tensor are clearly resolved at Q-band frequency (Fig. 4c). The same experiment carried out on a ^{17}O enriched zeolite leads to the complex spectral pattern shown in Fig. 4b and d, clearly showing the presence of an 11-line ^{17}O hyperfine pattern superimposed to the unlabelled Zn^+ spectrum [31].

The presence of an 11-line pattern calls for the interaction with two magnetically equivalent oxygens (Fig. 2b) and from the relative intensities of the three isotopomers the level of isotopic enrichment can be established (see Fig. 3). However, to achieve this, a reliable determination of the ^{17}O hyperfine tensor should be available, which is not easily extracted solely from the CW-EPR spectrum. From a methodological point of view, it is therefore important to extract the hyperfine
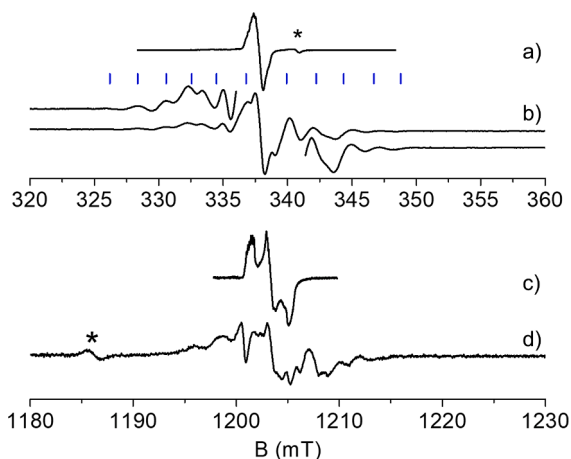

Fig. 4. Experimental X-band CW-EPR spectra of a) unlabelled Zn^I/ZSM-5 and b) ^{17}O enriched Zn^I/ZSM-5. Experimental Q-band CW-EPR spectra of c) unlabelled Zn^I/ZSM-5 and d) ^{17}O enriched Zn^I/ZSM-5. The asterisk in d marks a spurious baseline signal.

tensor accurately, a task readily accomplished by ENDOR/HYSCORE spectroscopies. In Fig. 5 representative Q-band Davies-ENDOR and HYSCORE spectra of Zn^I/ZSM-5 are reported. The Q-band Davies ENDOR spectrum (black trace in Fig. 5a) is characterized by a broad doublet separated by twice the ^{17}O Larmor frequency (6.93 MHz at 1.2 T) and centered at $A/2$. The asymmetry shown by the two doublets reflects the anisotropy of the hyperfine coupling while the unresolved nuclear quadrupole interaction contributes to the linewidth. Spectra taken at different field positions allow to recover the full ^{17}O hyperfine tensor, which is characterized by a large $|a_{iso}|$ of ≈ 50 MHz indicative of a σ-bonding interaction. The optimal choice of the operational frequency is important, as shown by the simulated spectra at X- and W-band frequencies. At X-band the lower nuclear Larmor frequency leads to an overlap between the transitions in the $m_S = -1/2$ and $m_S = 1/2$ electron spin manifold, which would result in an unresolved spectrum. Recording the spectrum at even higher MW frequency, for instance W-band frequency, is in general advantageous [47], although in this specific case one of the nuclear transitions falls in the low frequency region, which often suffers from poor sensitivity. Moreover, for air-sensitive powder samples, W-band capillaries are impractical leaving Q-band setup as an optimal compromise for the detection of ^{17}O hyperfine spectra.

While Davies ENDOR is ideally suited to detect the large ^{17}O hyperfine couplings, HYSCORE experiments complement the characterization by detecting small couplings in the weak-coupling regime $(2|\nu_I|>|A|)$. The Q-band ^{17}O-HYSCORE spectra taken at two different interpulse delays τ are shown in Fig. 5b. In the (-,+) quadrant cross-peaks are observed, which correspond to the large hyperfine couplings also detected in the ENDOR spectrum, while in the (+,+) quadrant a ridge with maximum extension of 9 MHz is clearly observed.

Analysis of all the ^{17}O EPR spectra (CW, ENDOR and HYSCORE) provides conclusive evidence that Zn^I species in zeolites are strongly bound to two equivalent oxygen donor atoms of the framework and weakly interacting with a third one. Moreover, the magnitude of the ^{17}O isotropic coupling (≈ 50 MHz) indicates a spin delocalization over the oxygen donor atoms of the order of 10%, which in turn stems from a non-negligible degree of covalency to the metal-oxygen bond. This observation is non-trivial especially considering the charged nature of the Zn^I species. Such large ^{17}O isotropic coupling can be taken as diagnostic of σ-type bonding as testified by similar values obtained in the case of Cu^{II} in ^{17}O enriched CHA [12] and ZSM-5 [48] zeolites.

The interaction between the transition metal 3d and the oxygen 2p orbitals via hybridization underpins many of the phenomena in transition metal oxide materials [49]. It is therefore interesting to evaluate the oxygen hybridization character, which can be described as sp^n with $n = (\rho_p/\rho_s)$. Using the atomic parameters of $a_0 = -4622.83$ MHz and $b_0 = 130.4$ MHz, which correspond to the hyperfine coupling predicted for unitary spin density in oxygen 2s and 2p orbitals [50], ρ_s and ρ_p can be estimated (Table 1) according to

$$\rho_s = \frac{a_{iso}}{a_0}\frac{g_e}{g_{iso}}; \; \rho_p = \frac{T}{b_0}\frac{g_e}{g_{iso}} \qquad (2)$$

where a_{iso} and T are the experimental isotropic and dipolar hyperfine couplings, g_e the free electron g value (2.0023) and $g_{iso} = 1/3(g_x+g_y+g_z)$ [14,31].

In the case of Zn and Cd, the oxygen hybridization ratio is close to 2 while for the Cu case is much higher, implying a 88.5% p character of the O—Cu σ-bond in this case. This is at stark difference with the case of N—Cu bonds such as those involving imidazole nitrogen ligands in the copper tetraphenylporphyrin (CuTPPP) complex. In this case, while the total spin density on the ligands is of the same order (about 35 for O—Cu bonds and 38 for N—Cu in Table 1), the hybridization ratio of the nitrogen is close to 2 implying a sp^2 hybrid character of the N—Cu σ-bond. The experimentally derived values nicely agree with the calculated Löwdin partition analysis of the spin density which provides
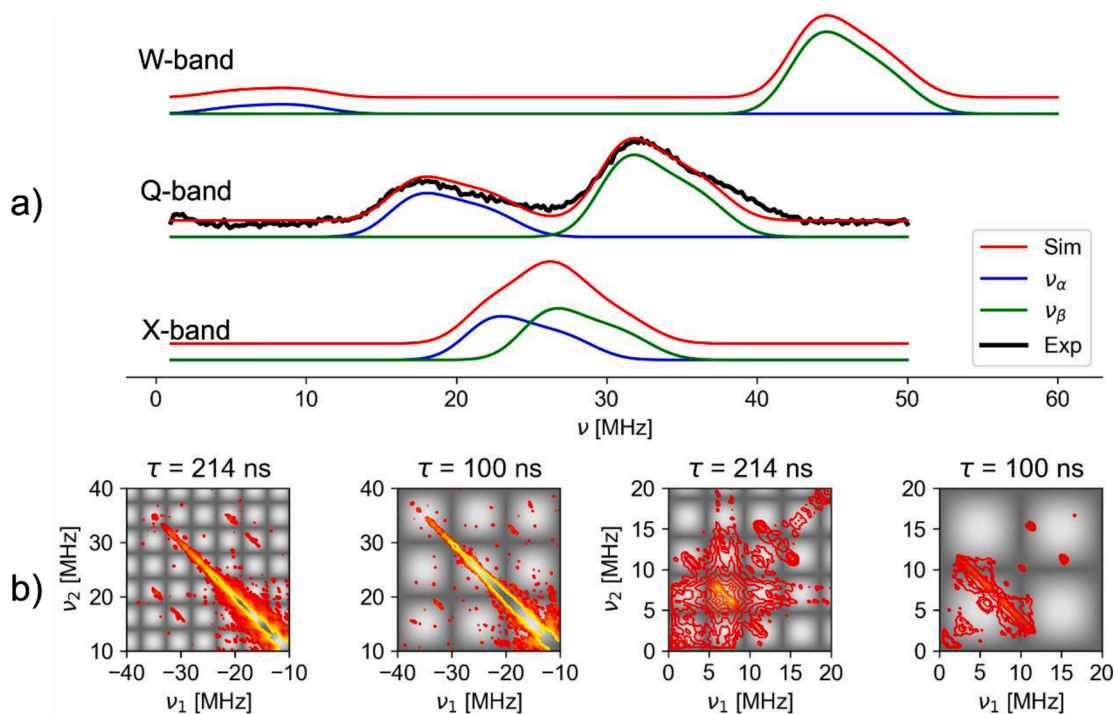
Fig. 5. a) Experimental (black) and simulated (red) Davies ENDOR spectra of ^{17}O enriched Zn^{I}/ZSM5. The blue and green lines simulate the nuclear transitions in the $m_S = -1/2$ and $m_S = \frac{1}{2}$ electron spin manifolds. b) Experimental Q-band HYSCORE spectra of ^{17}O enriched Zn^{I}/ZSM5. The spectra were recorded with the pulse sequence $\pi/2-\tau-\pi/2-t_1-\pi-t_2-\pi/2-\pi$-echo, applying a eight-step phase cycle for eliminating unwanted echoes. Microwave pulse lengths $t_{\pi/2} = 16$ ns, $t_{\pi} = 32$ ns, and a shot repetition rate of 0.5 kHz were used. The t_1 and t_2 time intervals were incremented in steps of 8 ns, starting from 200 ns giving a data matrix of 250×250 points. The time traces of the spectra were baseline corrected with a third-order polynomial, apodized with a Hamming window and zero filled. After two-dimensional Fourier transformation, the absolute value spectra were calculated. The grey shadow indicates the distribution of the blind spots for the two τ values reported on the top of each spectrum.

Table 1
Experimentally derived bonding parameters for the metal-zeolite complexes, calculated spin populations (%) at ligand atoms (ρ_L) as well as in 2 s (ρ_s) and 2p (ρ_p) orbitals, and spin hybridization coefficients ($n = \rho_p/\rho_s$). The data relative to nitrogen ligands are relative to CuTPP, taken from Brown and Hoffman [51].

		Zn	Cd	Cu
Oxygen	ρ_L	≈6	≈6	34.6
	ρ_s	1.1	0.86	1.1/0.87
	ρ_p	1.6	2.0	8.5/6.6
	n	1.45	2.3	7.7
Nitrogen	ρ_L	–	–	37.7
	ρ_s	–	–	3.05
	ρ_p	–	–	6.37
	n	–	–	2.09

hybridization parameters $n = 4.2$ and 3.9 for Zn and Cd respectively and a larger value $n = 8.7$ for Cu, where the difference appears to be related to the constrain imposed by the maximization of metal-oxygen orbital overlap when s and d orbitals are involved. Importantly, such a large difference in the p/s character is not reflected by a significant change in the geometry. Indeed, the Si-O-Al bonding angles of the different complexes (Fig. 7) remain in the range 137° (Cu) and 131° (Zn). This is in part due to the constraint imposed by the rigid framework and highlights that the p/s character of a bond is not simply determined by geometry, stressing the importance to determine the effective hybridization experimentally, and not to impose a value in advance.

3.4. Metal-oxygen π-bonding. V^{IV} in zeolites

A complementary scenario is offered by V^{IV} which is a $3d^1$ TMI also of relevance in catalysis.

Vanadium may be deposited within the zeolite framework through a number of ways. Among these, the evaporation of molecular precursors such as $VOCl_3$ or VCl_4 with low vapour tension are particularly well suited to generate isolated single sites [52,53]. We used this strategy to characterize the V-O interaction in a vanadium-exchanged H-ZSM-5 labelled with ^{17}O [54]. The formation of VO^{2+} isolated species was achieved by vapour exchange of $VCl_{4(g)}$. The CW-EPR spectra of the unlabelled and ^{17}O-labelled samples are virtually indistinguishable indicating that ^{17}O hyperfine interactions and the corresponding spin density delocalization are small. ^{17}O HYSCORE experiments at Q-band (Fig. 6a) reveal such interactions in term of cross-peaks centred at the ^{17}O Larmor frequency. The corresponding X-band HYSCORE spectrum is shown in Fig. 6b. In this case, the spectrum is dominated by the presence of cross-peaks in the (-,+) quadrant at approximately (−11, 3.5) MHz (−3.5, 11) MHz which can be ascribed to double-quantum transitions arising from the hyperfine interaction of the unpaired electron with a ^{17}O nucleus. Single-quantum transitions fall in the region between −2 and −6 MHz. Simulation of the spectra recorded at the two microwave frequencies revealed to be rather challenging and a reasonable agreement was obtained using the following set of spin-Hamiltonian parameters: $a_{iso} \approx 5.5 \pm 2$ MHz, $T \approx 0.5 \pm 0.5$ MHz and $e^2Qq/h \approx 9.5$ MHz. The simulation obtained by using these parameters are reported in Fig. 6c and d and indicate a a_{iso} value slightly larger than what reported previously by some of us [54], but in line with couplings assigned to equatorially bound oxygen atoms in pentacquo vanadyl complexes [41,55].

A positive sign is assigned to the isotropic hyperfine coupling (a_{iso}) in agreement with DFT calculations and NMR measurements on similar systems [41,55]. The a_{iso} term (Fermi contact term) arises from the finite probability of finding unpaired electron spin on an atomic s orbital. Given the negative gyromagnetic ratio γ of the ^{17}O nuclear spin, the positive sign of the *hfi* corresponds to a negative contribution of the spin
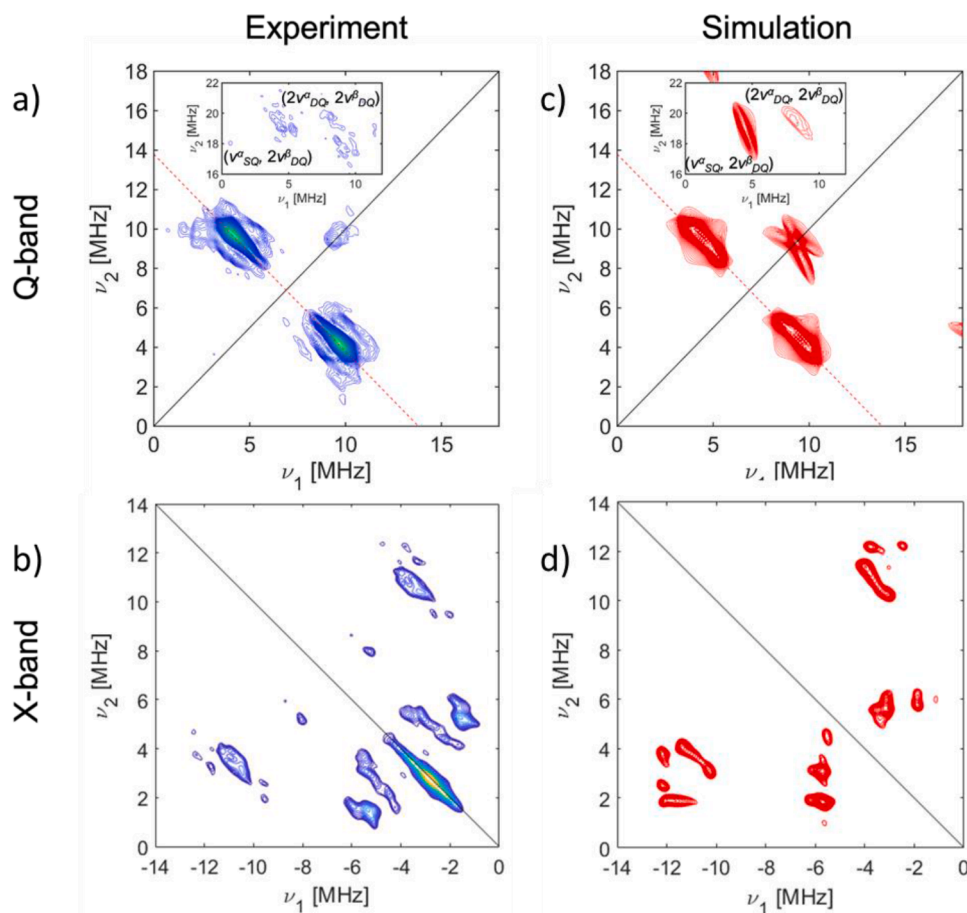
Fig. 6. Experimental Q- a) and X-band b) ^{17}O HYSCORE spectra of ^{17}O enriched $V^{IV}O$/ZSM-5. The Q-band spectrum was recorded at $B_0 = 1196.0$ mT with $\tau = 144$ ns, while the X-band spectrum was recorded at $B_0 = 354$ mT with $\tau = 144$ ns; Computer simulation of the corresponding Q- c) and X- band d) experimental spectra. The experimental spectra were recorded at $T = 30$ K.

distribution in the oxygen 2s orbital, which arises from the effective polarization induced by the unpaired electron spin density in the 2p orbitals perpendicular to the V-O bond. Indeed, the calculated spin density plot (Fig. 7b) graphically shows the negative spin density (blue) in the oxygen hybrid orbitals aligned along the V-O bonds and the positive (cyan) spin density in the p orbitals perpendicular to the bond. This is opposite to water coordination to nitroxide spin labels, where a negative a_{iso}(positive spin density at the oxygen) is observed because of a direct spin density transfer via overlap of the SOMO with the H atom of a hydrogen bonded water molecule [56].

If we focus on the magnitude of the spin-Hamiltonian parameters, it is immediately evident that for 3d^1 species the ^{17}O hyperfine interaction is one order of magnitude smaller with respect to 4s^1 species. This reflects a limited overlap between the metal 3d and oxygen 2p orbitals which, in turn, is characteristic of π-bond interaction. Similar values were reported for ^{17}O-labelled pentacquo vanadyl molecular complexes [43,55] but also for [Ti(H$_2$O)$_6$]$^{3+}$ complexes [57]. On the other hand, the ^{17}O hyperfine coupling for the $V = O$ vanadyl moiety has been reported to have a similar $a_{iso} = 8.4$ MHz but a much larger dipolar coupling ($T \approx 7.6$ MHz from [55]). This seems to be a common feature of the TMIs displaying sp^2-oxo bond. Indeed, similar values were found for other metal-oxo linkages, such as Mo=O [58].

4. Microscopic structures from ^{17}O hyperfine interactions and theoretical modelling

The ^{17}O hyperfine couplings of oxygen donor atoms coordinating the metal ion are diagnostic of its geometric structure, accounting even for

tiny structural differences [14]. The proper reproduction of these parameters with electronic structure methods thus ensures the translation of the spectroscopic fingerprints into microscopic structures. To this regard, in case of solid-state systems, the adoption of models featuring periodic boundary conditions and semi-empirical corrections for the dispersive interactions is essential to obtain a more reliable geometry with respect to a molecular cluster approach. Once obtained the relaxed periodic structure, the *hfi* couplings may be calculated by either extracting a cluster model (keeping the same geometry, multiplicity and charge as in the periodic model) or continuing with a periodic approach. Due to the localized nature of EPR properties, both the approaches lead to similar results as long as the size of the cluster model includes up to the third coordination sphere of the paramagnetic center.

Hybrid Density Functional Theory (DFT) methods provide a satisfactory description of the covalency of the metal-oxygen bonds in zeolites in most of the cases [14,31] and the calculated ^{17}O hyperfine couplings from the oxygen donor atoms directly coordinated to the metal ions are in reasonable agreement with the experimental values (Table 2). The negligibility of the spin-orbit component of the *hfi* as well as of the relativistic effects for lighter nuclei permits to achieve higher accuracy in predicting the hyperfine couplings of O ligands compared to the case of metal nuclei [39,59,60]. The calculation of the a_{iso}term remains challenging since it strongly depends on core-polarization effects which are difficult to model with high accuracy [61]. This can be partially mitigated by using specific basis sets rich of functions in the core region [28].

We remark that popular hybrid DFT functionals may exaggerate the spin delocalization over specific ligands (e.g. OH$^-$) leading to a
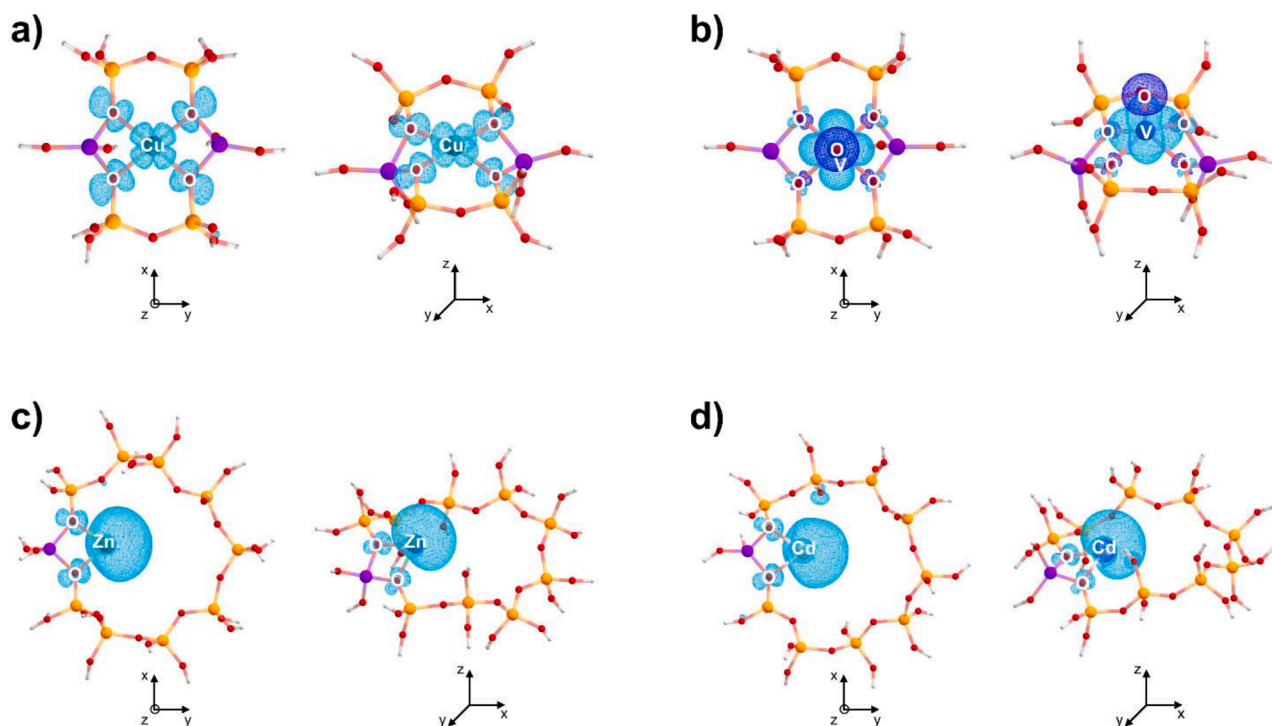
Fig. 7. Computed spin density distribution contoured at $\pm$ 0.002 electrons/a_0^3 (cyan = positive spin density; blue = negative spin density) for transition metal ions in ZSM-5 cluster models. a) Cu^{II}, b) V^{IV}O, c) Zn^{I}, d) Cd^{I}. The orientations of each cluster model are given by the reported cartesian axes. Si, O, Al and H atoms are shown in orange, red, violet and white, respectively.

Table 2
Comparison between computed and relevant experimental ^{17}O hyperfine couplings for oxygen donor atoms directly coordinated to the metal ions in ZSM-5 zeolite. The hyperfine couplings are given in MHz.

System		$|a_{iso}|$	$|T|$	Reference
Cu^{II}-O	Computed	45.6	18.6	This work
		45.2	17.3	
		47.1	18.9	
		44.0	17.3	
	Experimental	51.0	14.0	[48]
V^{IV}-O	Computed	3.7	3.4	This work
		3.4	2.7	
		3.1	3.1	
		3.2	3.3	
	Experimental	4.13	3.1	[54]
Zn^{I}-O	Computed	55.1	15.7	[31]
		55.5	17.0	
	Experimental	52.0	10.0	
Cd^{I}-O	Computed	45.2	13.7	[31]
		44.7	13.3	
	Experimental	40.0	10.0	

overestimation of *hfi* couplings. In those cases, it is crucial to adopt more expensive wave-function based methods such as Coupled Cluster with Single and Double excitations (CCSD) which yield a correct description of the spin density and, thus, of the hyperfine couplings (the interested reader is referred to [15]).

5. Outlook and conclusions

^{17}O hyperfine interactions between TMIs and surface oxygen atoms are key elements to establish correlations between the properties of molecular ligands and interfacial atoms for the design of structurally defined sites on surfaces for a range of applications. This link is exemplified by the hyperfine and nuclear quadrupole data reported in Table 3 for TMI-^{17}O bonds. In compiling Table 3 we did not limit to solid-state

systems, but we considered all the most recent and complete data available. The scope of Table 3 is to summarise all the data on ^{17}O hyperfine coupling currently available and help draw predictions regarding the nature of a binding site and the corresponding chemical bond. Examination of the reported data shows that for $S = 1/2$ species oxygen coordination via σ-bonding is characterized by large (negative, i. e. corresponding to a positive spin density at the oxygen donor atoms) Fermi contact terms of the order $|50$–$60|$ MHz while small and positive (corresponding to the presence of negative spin density) couplings of the order of 5–7 MHz are typically observed in the case of π-bonding interactions and provide *fingerprint* signatures to identify the different bonding channels. Nuclear quadrupole values for ^{17}O fall in a relatively narrow range spanning 3–11 MHz. The link between molecular and interfacial inorganic complexes is further emphasized by the computed spin density plots reported in Fig. 7, where the spin density delocalization for Cu^{II}, V^{IV}O, Zn^{I} and Cd^{I} are reported (see Table 2 for the corresponding spin-Hamiltonian derived parameters). These provide a convenient way to visualise and understand the experimental results. For instance, the 45° tilting of the lobes of the metal 3d orbitals from V^{IV}O (3d$_{xy}$ ground state) to Cu^{II} (3d$_{xy}^2$ ground state) graphically shows the origin of the different (one order of magnitude) ^{17}O *hfi* and indicate the shift from π- to σ-bonding interactions. The latter scenario implies a much larger delocalization of the electron spin over the oxygen donor atoms. In a similar way, σ-bonding interactions are afforded by Zn^{I} and Cd^{I} species featuring 4s and 5s ground states. Noteworthy, in the case of the softer and larger Cd atom, the spin density is predicted to delocalize over a greater number of oxygen atoms with respect to the Zn case, as experimentally observed [31].

The application of ^{17}O hyperfine spectroscopy has a huge potential in various areas of chemistry and materials science and we expect its application to grow in the future. In the case of surface chemistry and heterogeneous catalysis, we have shown that ^{17}O enrichment of the solid can be obtained in a relatively easy and economical way, relying on surface chemistry concepts, which allow the selective doping of the most active sites. Depending on the nature of the chemical interaction, ^{17}O

Table 3

^{17}O Spin-Hamiltonian parameters for oxygen atoms directly coordinated to metal ions. Hyperfine couplings and e^2qQ/h values are reported in MHz.

System		$|a_{iso}|$	$|T|$	$|e^2qQ/h|$	η	Comments	Reference
Ti^{III}(H$_2$O)$_6$		7.5	1	6	0.5	d$_z^2$ ground state	[57]
V^{IV}-O (TiO$_2$-solgel)		5.9	1.1	/	/	d$_{xy}$ ground state	[62]
V^{IV}-O (Zeolite)	hydroxyl group	4.13	3.1	9.5	0.2	d$_{xy}$ ground state	[54]
	framework			2	0		
V^{IV}=O(H$_2$O)$_5$	oxo	12.0	3.8	3.3	0.14	d$_{xy}$ ground state	[41]
	axial	5.0	1.45	10.7	0.59		
	equatorial	7.14	0.85	10.7	0.57		
V^{IV}=O(H$_2$O)$_5$	oxo	8.4	7.6	3.3	0.14	d$_{xy}$ ground state	[55]
	equatorial	7.16	0.42	10.7	0.52		
Cr^{V}=O(ditox)$_3$	oxo	9.8	3.2	0.8	/	d$_{xy}$/d$_{xy}^2$ ground state	[63]
Mo^{V}=O(high-pH sulfite oxidase)	oxo	6.3	1.7	1.5	1	d$_{xy}$ ground state	[58]
Mo^{V}-O(high-pH sulfite oxidase)	equatorial	37	2.5	/	/	d$_{xy}$ ground state	[64]
[Mo^{V}=O(SPh)4]$^-$	oxo	6.5	1.6	1.45	≤0.15	d$_{xy}$ ground state	[39]
Mn^{II}(H$_2$O)$_6$		7.5	1	6	1	high spin, $S = 5/2$	[55]
		7.5	1.2	7	1		[65]
		7.5	1.15	4	0		[41]
Mn^{III}-(μO)$_2$_Mn^{IV} BIPY	μ-oxo bridge	8.0	5.0	/	/	antiferromagnetic coupled Mn^{III}-Mn^{IV}	[43]
Mn$_4$O$_5$Ca (Photosystem II)	water/hydroxo	4.5	0.6	/	/	$S = 1/2$ ground state	
	water/hydroxo	1.4	0.6	/	/		
	μ-oxo bridge	9.7	2.2	/	/		
Fe^{III}-O (Enzyme P450cam)	axial water molecule	2.6	0.3	6.6	0.9	Low-spin Fe^{III} with d$_{yz}$ ground state	[66]
		0.4	1.8				
Fe^{IV}=O (Enzyme CPO-I)	oxo	67.0	65.0	< 6.0	/	d$_{xz}$/d$_{yz}$ ground state	[67]
Co^{II}-O-O (Vitamin B$_{12r}$)		82.0	85.0	/	/	d$_z^2$ ground state	[68]
		97.0	104.0	/	/		
Ni^{II}-O$_2$ (Zeolite)	superoxo	2.6	3.1	/	/	d$_z^2$ ground state	[69]
Cu^{II}(H$_2$O)$_6$	equatorial	43.8	19.1	/	/	d$_{xy}^2$ ground state	[70]
	axial	1.1	2.7	6.4	0.9		[71]
Cu^{II}-O (Zeolite)		51.0	24.0	< 7	0.9	d$_{xy}^2$ ground state	[14]
		41.0	19.0				
Zn^{I}-O (Zeolite)		52.0	10.0	/	/	s^1 ground state	[31]
		8.0	1.8	/	/		
		2.0	1.0	/	/		
Cd^{I}-O (Zeolite)		40.0	10.0	/	/	s^1 ground state	[31]
		29.0	10.0	/	/		
		21.0	4.0	/	/		
		8.0	1.8	/	/		
		2.0	1.0	/	/		
Gd^{III}-O (water complex)		0.75	0.69	6.5	1	f ground state	[72]

hyperfine couplings can span one order of magnitude in difference ranging from values of the order of few MHz up to 70 MHz for directly coordinated σ-bonded oxo ligands. This spread of values call for a careful choice of the experimental technique and operational frequency. While high frequencies are ideally suited to reduce quadrupole broadening and increase the orientational selectivity, they may suffer of lower sensitivity due to the spread of resonances due to *g*-anisotropy. HYSCORE is particularly versatile and well-suited especially at Q-band frequencies to detect couplings in the range 2–10 MHz. Davies-ENDOR, despite the lower sensitivity, was found to be ideally suited to detect the large couplings related to metal-oxygen σ-bonding. The combination of the two techniques (HYSCORE and Davies ENDOR) at Q-band has revealed to be outstandingly effective in recovering the full set of *hfi* couplings. A final comment concerns the relationship between ^{17}O hyperfine couplings and the coordination geometry of TMIs in zeolites and on surfaces in general. Orientational selective experiments allow to pinpoint the in plane and out of plane orientation of the ligands, while the spin density distribution provides particularly useful hints into the degree of covalency of the metal-oxygen bond. The use of computational techniques is indispensable to derive microscopic models. We remark that since ^{17}O *hfi* couplings are highly dependent on the geometric structure, reliable reproduction of these parameters, can reassure on the correct geometric description, strongly validating the computational model.

The use of ^{17}O hyperfine spectroscopy is gaining momentum in different domains of chemistry and its great potential is awaiting to be uncovered in the area of heterogeneous catalysis and surface chemistry.

Declaration of Competing Interest

The authors declare that they have no known competing financial interests or personal relationships that could have appeared to influence the work reported in this paper.

Data availability

Data will be made available upon acceptance within the Zenodo portal, in compliance with EU funded projects open access policies

References

[1] G. Pacchioni, Electronic interactions and charge transfers of metal atoms and clusters on oxide surfaces, Phys. Chem. Chem. Phys. 15 (2013) 1737–1757.
[2] S.K. Kaiser, Z. Chen, D. Faust Akl, S. Mitchell, J. Pérez-Ramírez, Single-atom catalysts across the periodic table, Chem. Rev. 120 (2020) 11703–11809.
[3] G. Pacchioni, H.-J. Freund, Controlling the charge state of supported nanoparticles in catalysis: lessons from model systems, Chem. Soc. Rev. 47 (2018) 8474–8502.

[4] S. Baumann, W. Paul, T. Choi, C.P. Lutz, A. Ardavan, A.J. Heinrich, Electron paramagnetic resonance of individual atoms on a surface, Science 350 (2015) 417–420.

[5] P. Willke, Y. Bae, K. Yang, J.L. Lado, A. Ferrón, T. Choi, A. Ardavan, J. Fernández-Rossier, A.J. Heinrich, C.P. Lutz, Hyperfine interaction of individual atoms on a surface, Science 362 (2018) 336–339.

[6] S. Kovarik, R. Robles, R. Schlitz, T.S. Seifert, N. Lorente, P. Gambardella, S. Stepanow, Electron paramagnetic resonance of alkali metal atoms and dimers on ultrathin MgO, Nano Lett. 22 (2022) 4176–4181.

[7] L. Farinacci, L.M. Veldman, P. Willke, S. Otte, Experimental determination of a single atom ground state orbital through hyperfine anisotropy, Nano Lett. 22 (2022) 8470–8474.

[8] F.J. Adrian, Guidelines for interpreting electron spin resonance spectra of paramagnetic species adsorbed on surfaces, J. Colloid Interface Sci. 26 (1968) 317–354.

[9] K.M. Wang, J.H. Lunsford, Electron paramagnetic resonance evidence for the presence of aluminum at adsorption sites on decationated zeolites, J. Phys. Chem. 73 (1969) 2069–2071.

[10] K. Dyrek, M. Che, EPR as a tool to investigate the transition metal chemistry on oxide surfaces, Chem. Rev. 97 (1997) 305–332.

[11] W. Weltner, Magnetic Atoms and Molecules, Dover Publications, New York, 1989.

[12] E. Salvadori, P.C. Bruzzese, E. Giamello, M. Chiesa, Single metal atoms on oxide surfaces: assessing the chemical bond through ^{17}O electron paramagnetic resonance, Acc. Chem. Res. 55 (2022) 3706–3715.

[13] M. Hartmann, L. Kevan, Transition-metal ions in aluminophosphate and silicoaluminophosphate molecular sieves: location, interaction with adsorbates and catalytic properties, Chem. Rev. 99 (1999) 635–664.

[14] P.C. Bruzzese, E. Salvadori, S. Jäger, M. Hartmann, B. Civalleri, A. Pöppl, M. Chiesa, ^{17}O-EPR determination of the structure and dynamics of copper single-metal sites in zeolites, Nat. Commun. 12 (2021) 4638.

[15] P.C. Bruzzese, E. Salvadori, S. Jäger, M. Hartmann, A. Pöppl, M. Chiesa, The structure of monomeric Hydroxo-Cu^{II} species in Cu-CHA. A quantitative assessment, J. Am. Chem. Soc. 144 (2022) 13079–13083.

[16] S. Stoll, A. Schweiger, EasySpin, a comprehensive software package for spectral simulation and analysis in EPR, J. Magn. Reson. 178 (2006) 42–55.

[17] G. Artioli, C. Lamberti, G.L. Marra, Neutron powder diffraction study of orthorhombic and monoclinic defective silicalite, Acta Crystallogr. Sect. B. 56 (2000) 2–10.

[18] R. Dovesi, A. Erba, R. Orlando, C.M. Zicovich-Wilson, B. Civalleri, L. Maschio, M. Rérat, S. Casassa, S. Baima, S. Salustro, B. Kirtman, Quantum-mechanical condensed matter simulations with CRYSTAL, Wiley Interdiscip. Rev. Comput. Mol. Sci. 8 (2018) e1360.

[19] R. Orlando, M. Delle Piane, I.J. Bush, P. Ugliengo, M. Ferrabone, R. Dovesi, A new massively parallel version of CRYSTAL for large systems on high performance computing architectures, J. Comput. Chem. 33 (2012) 2276–2284.

[20] A. Erba, J. Baima, I. Bush, R. Orlando, R. Dovesi, Large-scale condensed matter DFT simulations: performance and capabilities of the crystal code, J. Chem. Theory Comput. 13 (2017) 5019–5027.

[21] C. Lee, W. Yang, R.G. Parr, Development of the Colle-Salvetti correlation-energy formula into a functional of the electron density, Phys. Rev. B. 37 (1988) 785–789.

[22] A.D. Becke, Density-functional thermochemistry. III. The role of exact exchange, J. Chem. Phys. 98 (1993) 5648–5652.

[23] S. Grimme, J. Antony, S. Ehrlich, H. Krieg, A consistent and accurate ab initio parametrization of density functional dispersion correction (DFT-D) for the 94 elements H-Pu, J. Chem. Phys. 132 (2010), 154104.

[24] S. Grimme, S. Ehrlich, L. Goerigk, Effect of the damping function in dispersion corrected density functional theory, J. Comput. Chem. 32 (2011) 1456–1465.

[25] D. Vilela Oliveira, J. Laun, M.F. Peintinger, T. Bredow, BSSE-correction scheme for consistent gaussian basis sets of double- and triple-zeta valence with polarization quality for solid-state calculations, J. Comput. Chem. 40 (2019) 2364–2376.

[26] F. Neese, Software update: the ORCA program system—version 5.0, Wiley Interdiscip. Rev. Comput. Mol. Sci. (2022) e1606.

[27] S. Sinnecker, L.D. Slep, E. Bill, F. Neese, Performance of nonrelativistic and quasi-relativistic hybrid DFT for the prediction of electric and magnetic hyperfine parameters in ^{57}Fe mössbauer spectra, Inorg. Chem. 44 (2005) 2245–2254.

[28] V. Barone, Structure, thermochemistry, and magnetic properties of binary copper carbonyls by a density-functional approach, J. Phys. Chem. 99 (1995) 11659–11666.

[29] F. Weigend, R. Ahlrichs, Balanced basis sets of split valence, triple zeta valence and quadruple zeta valence quality for H to Rn: design and assessment of accuracy, Phys. Chem. Chem. Phys. 7 (2005) 3297–3305.

[30] B.A. Heß, C.M. Marian, U. Wahlgren, O. Gropen, A mean-field spin-orbit method applicable to correlated wavefunctions, Chem. Phys. Lett. 251 (1996) 365–371.

[31] E. Morra, M. Signorile, E. Salvadori, S. Bordiga, E. Giamello, M. Chiesa, Nature and topology of metal–oxygen binding sites in zeolite materials: ^{17}O high-resolution EPR spectroscopy of metal-loaded ZSM-5, Angew. Chem. Int. Ed. 58 (2019) 12398.

[32] S.E. Ashbrook, Z.H. Davis, R.E. Morris, C.M. Rice, ^{17}O NMR spectroscopy of crystalline microporous materials, Chem. Sci. 12 (2021) 5016–5036.

[33] M. Chiesa, E. Giamello, M.C. Paganini, Z. Sojka, D.M. Murphy, Continuous wave electron paramagnetic resonance investigation of the hyperfine structure of $^{17}O_2-$ adsorbed on the MgO surface, J. Chem. Phys. 116 (2002) 4266–4274.

[34] J.R. Harmer, Hyperfine Spectroscopy – ENDOR, in: R. K. Harris and R. L. Wasylishen (Eds.), EMagRes, Chichester, 2016, pp. 1493–1514.

[35] S. Stoll, D. Goldfarb, EPR Interactions - Nuclear Quadrupole Couplings, in: R. K. Harris and R. L. Wasylishen (Eds.), EMagRes, Chichester, 2017, pp. 495–510.

[36] J. Telser, M.H. Emptage, H. Merkle, M.C. Kennedy, H. Beinert, B.M. Hoffman, ^{17}O electron nuclear double resonance characterization of substrate binding to the $[4Fe-4S]^{1+}$ cluster of reduced active aconitase, J. Biol. Chem. 261 (1986) 4840–4846.

[37] S. Van Doorslaer, Hyperfine Spectroscopy: ESEEM, in: R. K. Harris and R. L. Wasylishen (Eds.), EMagRes, Chichester, 2017, pp. 51–70.

[38] P. Höfer, A. Grupp, H. Nebenführ, M. Mehring, Hyperfine sublevel correlation (hyscore) spectroscopy: a 2D ESR investigation of the squaric acid radical, Chem. Phys. Lett. 132 (1986) 279–282.

[39] A.V. Astashkin, F. Neese, A.M. Raitsimring, J.J.A. Cooney, E. Bultman, J. H. Enemark, Pulsed EPR investigations of systems modeling molybdenum enzymes: hyperfine and quadrupole parameters of Oxo-^{17}O in $[Mo^{17}O(SPh)_4]^-$, J. Am. Chem. Soc. 127 (2005) 16713–16722.

[40] P. Schosseler, T. Wacker, A. Schweiger, Pulsed ELDOR detected NMR, Chem. Phys. Lett. 224 (1994) 319–324.

[41] N. Cox, W. Lubitz, A. Savitsky, W-band ELDOR-detected NMR (EDNMR) spectroscopy as a versatile technique for the characterisation of transition metal–ligand interactions, Mol. Phys. 111 (2013) 2788–2808.

[42] D. Goldfarb, ELDOR-Detected NMR, in: R. K. Harris and R. L. Wasylishen (Eds.), EMagRes, 2017, pp. 101–114.

[43] L. Rapatskiy, N. Cox, A. Savitsky, W.M. Ames, J. Sander, M.M. Nowaczyk, M. Rögner, A. Boussac, F. Neese, J. Messinger, W. Lubitz, Detection of the water-binding sites of the oxygen-evolving complex of photosystem II using W-Band ^{17}O electron–electron double resonance-detected NMR spectroscopy, J. Am. Chem. Soc. 134 (2012) 16619–16634.

[44] T. Hetzke, A.M. Bowen, T.F. Prisner, ELDOR-detected NMR at Q-Band, Appl. Magn. Reson. 48 (2017) 1375–1397.

[45] E. Morra, G. Berlier, E. Borfecchia, S. Bordiga, P. Beato, M. Chiesa, Electronic and geometrical structure of Zn^+ ions stabilized in the porous structure of Zn-loaded zeolite H-ZSM-5: a multifrequency CW and Pulse EPR study, J. Phys. Chem. C. 121 (2017) 14238–14245.

[46] E. Morra, M. Chiesa, Chemically induced formation of monovalent Cd^+ ions and reversible O_2 activation in cadmium-loaded ZSM-5 zeolite, J. Phys. Chem. C. 122 (2018) 9515–9522.

[47] P.J. Carl, D.E.W. Vaughan, D. Goldfarb, High field ^{27}Al ENDOR reveals the coordination mode of Cu^{2+} in low Si/Al zeolites, J. Am. Chem. Soc. 128 (2006) 7160–7161.

[48] A. Actis, E. Salvadori, M. Chiesa, Framework coordination of single-ion Cu^{2+} sites in hydrated ^{17}O-ZSM-5 zeolite, Catal. Sci. Technol. 11 (2021) 5191–5199.

[49] J. Suntivich, W.T. Hong, Y.-L. Lee, J.M. Rondinelli, W. Yang, J.B. Goodenough, B. Dabrowski, J.W. Freeland, Y. Shao-Horn, Estimating hybridization of transition metal and oxygen states in perovskites from O K-edge X-ray absorption spectroscopy, J. Phys. Chem. C. 118 (2014) 1856–1863.

[50] J.A.J. Fitzpatrick, F.R. Manby, C.M. Western, The interpretation of molecular magnetic hyperfine interactions, J. Chem. Phys. 122 (2005), 084312.

[51] T.G. Brown, B.M. Hoffman, ^{14}N, ^1H, and metal ENDOR of single crystal Ag(II)(TPP) and Cu(II)(TPP), Mol. Phys. 39 (1980) 1073–1109.

[52] H.S. Lacheen, E. Iglesia, Synthesis, structure, and catalytic reactivity of isolated V^5+-oxo species prepared by sublimation of $VOCl_3$ onto H-ZSM5, J. Phys. Chem. B. 110 (2006) 5462–5472.

[53] H.S. Lacheen, E. Iglesia, Structure of zirconium-exchanged H-ZSM5 prepared by vapor exchange of $ZrCl_4$, Chem. Mater. 19 (2007) 1877–1882.

[54] V. Lagostina, E. Salvadori, M. Chiesa, E. Giamello, Electron paramagnetic resonance study of vanadium exchanged H-ZSM5 prepared by vapor reaction of VCl_4. The role of ^{17}O isotope labelling in the characterisation of the metal oxide interaction, J. Catal. 391 (2020) 397–403.

[55] J. Telser, H.-I. Lee, E. Hoffman, Hyperfine and quadrupole interactions for the hexaaquovanadium(III) ion $(H_2^{17}O)_6^{2+}$ determined by high field ENDOR aided by DFT calculations, J. Phys. Chem. A. 109 (2005) 7865–7871.

[56] F. Hecker, L. Fries, M. Hiller, M. Chiesa, M. Bennati, ^{17}O hyperfine spectroscopy reveals hydration structure of nitroxide radicals in aqueous solutions, Angew. Chem. Int. Ed. (2022), e202213700 n/a.

[57] S. Maurelli, S. Livraghi, M. Chiesa, E. Giamello, S. Van Doorslaer, C. Di Valentin, G. Pacchioni, Hydration structure of the Ti(III) cation as revealed by pulse EPR and DFT studies: new insights into a textbook case, Inorg. Chem. 50 (2011) 2385–2394.

[58] A.V. Astashkin, Feng, A.M. Raitsimring, J.H. Enemark, ^{17}O ESEEM evidence for exchange of the axial oxo ligand in the molybdenum center of the high pH form of sulfite oxidase, J. Am. Chem. Soc. 127 (2005) 502–503.

[59] M.M. Cosper, F. Neese, A.V. Astashkin, M.D. Carducci, A.M. Raitsimring, J. H. Enemark, Determination of the g-tensors and their orientations for cis,trans-(L-N_2S_2)Mo^VOX (X = Cl, SCH_2Ph) by single-crystal EPR spectroscopy and molecular orbital calculations, Inorg. Chem. 44 (2005) 1290–1301.

[60] J. Fritscher, P. Hrobárik, M. Kaupp, Computational studies of electron paramagnetic resonance parameters for paramagnetic molybdenum complexes. 1. Method validation on small and medium-sized systems, J. Phys. Chem. B. 111 (2007) 4616–4629.

[61] F. Neese, Prediction of molecular properties and molecular spectroscopy with density functional theory: from fundamental theory to exchange-coupling, Coord. Chem. Rev. 253 (2009) 526–563.

[62] V. Lagostina, E. Romeo, A. Maria Ferrari, V. Maurino, M. Chiesa, Monomeric (VO^2+) and dimeric mixed valence (V$_2$O$_3^{3+}$) vanadium species at the surface of shape controlled TiO_2 anatase nano crystals, J. Catal. 406 (2022) 28–38.

[63] T.A. Stich, D.M. Gagnon, B.L. Anderson, D.G. Nocera, R.D. Britt, EPR spectroscopic characterization of a Jahn-Teller distorted ($C_{3v} \rightarrow C_s$) four-coordinate chromium(V) oxo species, Isr. J. Chem. 56 (2016) 864–871.

[64] A.V. Astashkin, E.L. Klein, D. Ganyushin, K. Johnson-Winters, F. Neese, U. Kappler, J.H. Enemark, Exchangeable oxygens in the vicinity of the molybdenum center of the high-pH form of sulfite oxidase and sulfite dehydrogenase, Phys. Chem. Chem. Phys. 11 (2009) 6733–6742.

[65] X. Tan, M. Bernardo, H. Thomann, C.P. Scholes, [17]O hyperfine and quadrupole interactions for water ligands in frozen solutions of high spin Mn^{2+}, J. Chem. Phys. 102 (1995) 2675–2690.

[66] H. Thomann, M. Bernardo, D. Goldfarb, P.M.H. Kroneck, V. Ullrich, Evidence for water binding to the Fe center in cytochrome P450cam obtained by [17]O electron spin-echo envelope modulation spectroscopy, J. Am. Chem. Soc. 117 (1995) 8243–8251.

[67] M.J. Field, P.H. Oyala, M.T. Green, [17]O electron nuclear double resonance analysis of compound I: inverse correlation between oxygen spin population and electron donation, J. Am. Chem. Soc. 144 (2022) 19272–19283.

[68] E. Joerin, A. Schweiger, H.H. Guenthard, Single-crystal EPR of the [17]O-enriched dioxygen adduct of vitamin B_{12r}: reversible oxygen bonding, electronic and geometric structure and molecular dynamics, J. Am. Chem. Soc. 105 (1983) 4277–4286.

[69] P. Pietrzyk, K. Podolska, T. Mazur, Z. Sojka, Heterogeneous binding of dioxygen: EPR and DFT evidence for side-on nickel(II)–superoxo adduct with unprecedented magnetic structure hosted in MFI zeolite, J. Am. Chem. Soc. 133 (2011) 19931–19943.

[70] D. Getz, B.L. Silver, ESR of $Cu^{2+}(H_2O)_6$. I. The oxygen-17 superhyperfine tensors in $^{63}Cu^{2+}$ doped zinc tutton's salt at 20 °K, J. Chem. Phys. 61 (1974) 630–637.

[71] M.J. Colaneri, J. Vitali, Probing axial water bound to copper in tutton salt using single crystal [17]O-ESEEM spectroscopy, J. Phys. Chem. A. 122 (2018) 6214–6224.

[72] A.M. Raitsimring, A.V. Astashkin, D. Baute, D. Goldfarb, P. Caravan, W-Band [17]O pulsed electron nuclear double resonance study of gadolinium complexes with water, J. Phys. Chem. A. 108 (2004) 7318–7323.